Measurement of the imaginary part of the I=1 N-barN S-wave scattering length

Mutchler, G. S.; Clement, J.; Kruk, J.; Moss, R.; Hungerford, Ed V.; Kishimoto, T.; Mayes, B.; Pinsky, L.; Tang, L.; Xue, Y.; ...

Source / Izvornik: **Physical Review D, Particles and fields, 1988, 38, 742 - 753**

Journal article, Published version
Rad u časopisu, Objavljena verzija rada (izdavačev PDF)

https://doi.org/10.1103/PhysRevD.38.742

Permanent link / Trajna poveznica: https://urn.nsk.hr/urn:nbn:hr:217:059029

Measurement of the imaginary part of the $I=1$ $\bar{N}N$ S-wave scattering length

G. S. Mutchler, J. Clement, J. Kruk, and R. Moss
T. W. Bonner Nuclear Laboratories, Physics Department, Rice University, Houston, Texas 77251-1892

E. Hungerford, T. Kishimoto, B. Mayes, L. Pinsky, L. Tang, and Y. Xue
Physics Department, University of Houston, Houston, Texas 77004

B. Bassalleck
Physics Department, University of New Mexico, Albuquerque, New Mexico 87131

T. Armstrong, K. Hartman, A. Hicks, R. Lewis, W. Lochstet, and G. A. Smith
Laboratory for Elementary Particle Science, Physics Department, Pennsylvania State University, University Park, Pennsylvania 16802

D. Lowenstein
Brookhaven National Laboratory, Upton, New York 11973

H. Poth
Kernforschungzentrum, Karlsruhe Institut für Kernphysik, Karlsruhe, Federal Republic of Germany

W. von Witsch
Institut für Strahlen und Kernphysik, Der Universität Bonn, Bonn, Federal Republic of Germany

M. Furic
Faculty of Science, Department of Physics, University of Zagreb, Zagreb, Yugoslavia

(Received 5 February 1988)

The survival time spectrum of slow antineutrons produced in a liquid-hydrogen target has been measured. From these data the imaginary part of the $I=1$ spin-averaged S-wave antineutron proton scattering length has been deduced to be $\mathrm{Im}a_1=-0.83\pm0.07$ fm. The result lies within the range of values calculated from current potential models. In addition, by combining a_1 with the antiproton-proton scattering length deduced from antiprotonic atoms, the imaginary part of the $I=0$ spin-averaged $\bar{N}N$ scattering length was calculated to be $\mathrm{Im}a_0=-1.07\pm0.16$ fm.

I. INTRODUCTION

The study of the antinucleon-nucleon interaction at low energy has gained considerable interest since intense antiproton beams have become available. The theoretical approach to the problem is to describe the $N\bar{N}$ interaction at low energy in terms of a potential model with its real part derived from a microscopic NN potential by a G-parity transformation.[1] The $N\bar{N}$ potential constructed in this way is supplemented with an empirical imaginary part which accounts for the annihilation. The role of the annihilation in low-energy antinucleon-nucleon interactions is of great importance in a variety of contexts. For instance, it determines whether $N\bar{N}$ bound and resonant states exist.[2]

A key quantity characterizing any potential is the S-wave scattering length. All the models give definite predictions for this quantity, which is complex in the $N\bar{N}$ case. The antiproton-proton S-wave scattering length can be determined from the energy and the lifetime of the $1S$ state in antiprotonic hydrogen.[3-5] The determination of the antiproton-neutron scattering length is more difficult. It can be extracted from the analysis of energy shifts and widths of heavier antiprotonic atoms. One relies there on nuclear models, although these uncertainties can be reduced by the measurement of isotope effects.[6] The antineutron-proton interaction provides, in contrast with the antiproton-proton interaction, a cleaner situation since Coulomb effects are absent and the system is in a pure isospin ($I=1$) state. Hence, it is desirable to obtain independent information on the antineutron-proton interaction at low energy. Unfortunately, this system cannot easily be investigated at rest since, unlike antiprotons, antineutrons cannot be stopped and captured into atomic orbits. There are currently no direct measurements of the antineutron-proton scattering length. There are only two $\bar{n}p$ measurements, the first by Gunderson *et al.*[7] who measured the annihilation cross sections down to 250 MeV/c and the second by Armstrong *et al.*[8] down to 105 MeV/c. In addition there are two measurements of $\bar{p}n$ annihilation cross sections from $\bar{p}D$ interactions, one by Bizzari *et al.*[9] down to 333 MeV/c and the other by Kalogeropoulos and Tzanakos[10] down to 270 MeV/c.

We have applied a method originally proposed by Rosner[11] to investigate the antineutron-proton interaction down to very low energies. The method consists of converting antiprotons through charge exchange ($p+\bar{p} \rightarrow n+\bar{n}$) in a liquid-hydrogen ($LH_2$) target into antineutrons and measuring their survival time in the same target. The survival time of the antineutrons depends on the $\bar{n}p$ annihilation cross section at low energy. If only S waves are present the cross section is proportional to β^{-1} and $\beta\sigma$ approaches a constant as $\beta \rightarrow 0$. The basic concept of the experiment is illustrated in Fig. 1. A low-energy $\bar{n}$ is produced in a large LH_2 target by the $\bar{p}p \rightarrow \bar{n}n$ charge-exchange reaction. The kinematics of the charge-exchange reaction are shown in Fig. 2. Because of larger neutron mass, the reaction threshold is 5 MeV above the two proton masses which corresponds to 98-MeV/c antiproton laboratory momentum. The neutron (antineutron) momentum is symmetric about half of this value. Thus a fast forward-going neutron signals the creation of a low-energy $\bar{n}$. If the angle and momentum of the neutron are measured, the energy of the incident $\bar{p}$ and the created $\bar{n}$ can be calculated. The low-energy $\bar{n}$ then scatters in the LH_2 target until it annihilates or escapes. A measurement of the $\bar{n}$ survival time thus provides a measure of the low-energy annihilation cross section. In turn the elastic cross section $\sigma_E(0)$ and the annihilation cross section $\sigma_A(0)$ can be related to the complex $I=1$ scattering amplitude f via

$$\sigma_E(0)=\pi(|f_s|^2+3|f_t|^2) \text{ fm}^2 , \quad (1)$$

$$\sigma_A(0)=\frac{-\pi \operatorname{Im}(f_s+3f_t)}{k_{\text{c.m.}}} \text{ fm}^2 , \quad (2)$$

or

$$\beta\sigma_A(0)=-\frac{20\pi\hbar \operatorname{Im}(f_s+3f_t)}{Mc} \text{ mb} , \quad (3)$$

where β is evaluated in the laboratory system and f_s, f_t are, respectively, the spin-singlet and -triplet amplitudes. At sufficiently low energies, the scattering amplitude can be approximated by the scattering length a, defined by

$$k \cot\delta = -1/a, \quad \lim k \rightarrow 0 . \quad (4)$$

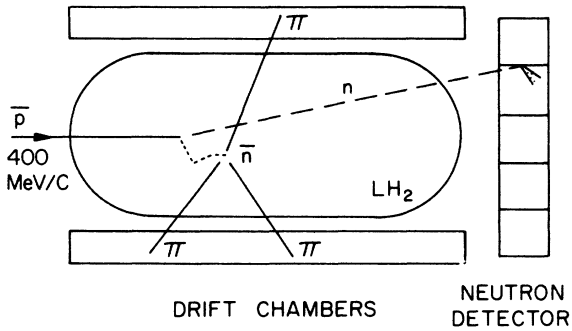

FIG. 1. Schematic diagram of experiment. The 400-MeV/c $\bar{p}$ charge exchanges in the liquid-hydrogen (LH_2) target. The forward-going neutron is detected in the neutron detector. The antineutron is produced at back angles (c.m.) and scatters in the LH_2 until it annihilates. The annihilation products are detected in the vertex detectors (drift chambers).

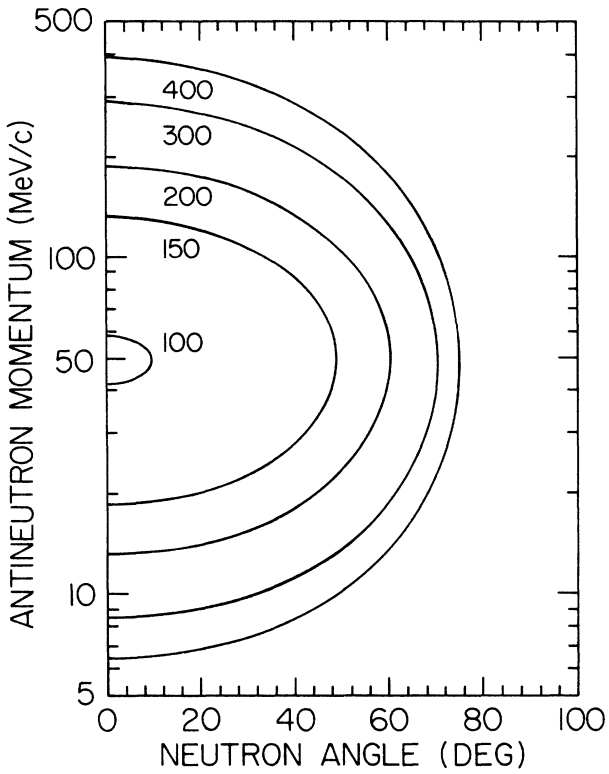

FIG. 2. $\bar{p}p \rightarrow \bar{n}n$ kinematics. A plot of antineutron laboratory momentum vs neutron laboratory angles. Each curve is labeled with the incident $\bar{p}$ momentum.

The quantity of interest, $\beta\sigma_A$, may be written in terms of the antineutron survival time in an infinite liquid-hydrogen target through the relationship[11]

$$\tau=\frac{790 \text{ mb ns}}{\beta\sigma_A} . \quad (5)$$

Hence a measurement of τ, the mean lifetime against annihilation, would yield $\beta\sigma_A$ directly. However, this relationship only applies if the annihilation cross section is proportional to $1/v$ (as would be the case for thermal antineutrons). In the present case, the antineutrons are generated with a mean momentum of 40 MeV/c and do not readily thermalize due to the large annihilation cross section, so what is actually measured is $dN_A(t)/dt$: the rate of annihilation versus time. This quantity depends on the position, energy, and angular distribution of the charge exchange, as well as the geometry of the finite liquid-hydrogen target. It also depends weakly, on the $\bar{n}p$ elastic cross section.

II. EXPERIMENTAL SETUP

The apparatus is shown in Fig. 3. The experiment was carried out in the C8 branch of the low-energy separated beam (LESB II) at the Brookhaven National Laboratory AGS. The central transport momentum was 415 MeV/c, with a $\Delta p/p$ acceptance of 4% full width at half maximum (FWHM). The beam intensity varied from 1500 to 3000 antiprotons per 1-s spill, with a pion contamination

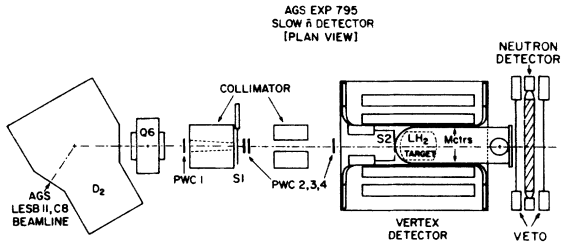

FIG. 3. Experimental setup. PWC1–4 are multiwire proportional chambers used to measure the antiproton beam phase space. Scintillators *BH* (not shown), *S*1, and *S*2 determine the $\bar{p}$ TOF and pulse height. LH_2 is a 45-liter liquid-hydrogen target. *M* counters are a twelve-sided array of scintillation counters, that serve as the fast trigger for the vertex detector. The neutron detector consists of eight scintillator bars.

that varied from 60:1 to 120:1. During the experiment approximately 3.9×10^9 antiprotons were collected in 1200 h of running.

Beam antiprotons were identified by time-of-flight (TOF) between counters *BH* and *S*1, as well as by their energy loss in counters *S*1 and *S*2. *BH* was a hodoscope of ten counters in the beam upstream of the final beamline bending magnet. The difference in time of flight between pions and antiprotons was 20 ns, which greatly exceeded the fluctuations due to the large momentum bite and variations in flight path length. The scintillator *S*2, 17.8×17.8 cm^2, was placed in contact with the forward edge of the target vacuum jacket, 5 cm from the LH_2. *S*2 was viewed by two photomultiplier tubes. The beam phase space was determined using four multiwire proportional chambers (PWC1–4) arranged as shown in Fig. 3. Each chamber contained an *x* and *y* coordinate sense wire plane with 2.5 mm wire spacing. On-line ray tracing was used to focus the beam in the LH_2 target. The beam spot was extrapolated to be 8.9×8.9 cm^2 FWHM at the center of the target.

The hydrogen target flask was a cylinder 35 cm long with a diameter of 40 cm. The cylinder was closed on each end by spherical caps with a radius of 30.5 cm. The longest dimension of the target was 50 cm. The walls of the cylinder (end caps) were 0.10 (0.08) cm of Mylar. Further details of the target are given in Ref. 12. The LH_2 target was surrounded by the vertex detector consisting of twelve scintillation counters (*M*1–*M*12) arranged in a "barrel stave" fashion and four quadrants of two drift chambers each. The *M* counters were 100×15 cm^2 and were viewed by a photomultiplier tube at each end. Acrylic light guides extended to the ends of the vacuum vessel. The average time from the two phototubes was used to give the time of hit, with a resolution of 1.4 ns FWHM, while the difference of the two times could be related to the position of the hit along the *M* counter with a resolution of ±5 cm. Immediately surrounding the *M* counters were four quadrants of two drift chambers each. Each quadrant contained an inner smaller chamber, of active area 56×151 cm^2, and an outer larger chamber of active area 107×151 cm^2. Each chamber contained four coordinate planes *U*, *X*1, *X*2, and *Y*. The innermost (nearest the LH_2 target) was a *U* coordinate with sense wires running at a 45° angle with respect to the chamber sides. The *X*1 and *X*2 coordinates had wires running perpendicular to the beam direction and were staggered by one-half sense-wire spacing with respect to each other. The *Y* coordinate had wires running parallel to the beam direction. The sense-wire-to-sense-wire spacing on all coordinates was 5.08 cm. The position resolution was a function of the incident track angle, but in general was better than ±1 mm for all reconstruction angles. Further details are given in Ref. 13.

The neutron detector consisted of eight scintillator bars $100\times20\times10$ cm^3. Each bar was coupled to two 5-in. Amperex 58 AVP or RCA Quantacon photomultipliers by Lucite Winston cone light guides. The mean time gave the neutron time of flight (TOF) with a resolution of 0.75 ns FWHM, while the time difference gave the *X* position with an uncertainty of about ±5 cm. The bars were positioned horizontally in two planes, with adjacent bars in alternate planes, 170 and 193 cm from their front face to the target center, respectively. The photomultipliers had high rate capability bases to withstand the high beam flux and background rates. The central bars had singles rates of approximately 1 MHz. Charged-particle veto paddles were positioned in front of and behind the neutron counters. The neutron counter pulse heights were calibrated using the incident beam pions which deposited 40-MeV energy in the 20-cm thickness, and minimally ionizing cosmic rays that deposited 20-MeV energy in the 10-cm vertical dimension. The threshold was set to 100-keV electron equivalent pulse height, which resulted in a minimum detectable neutron energy of 1 MeV. Using beam pions, a mean-time resolution of $\sigma_T\simeq300$ ps and a pulse-height resolution of $\sigma_E/E\simeq9\%$ was measured.

III. TRIGGER LOGIC AND ELECTRONICS

Data were collected by an on-line CAMAC data acquisition system and a DEC PDP 11/34 minicomputer. Standard NIM fast electronic modules were used for the trigger logic. The time and pulse height for *S*1, *S*2, *M* counters, and *N* counters were read out to tape. Constant fraction discriminators were used on these scintillators. Only the time information on the veto paddles and *BH* counters was read out. The drift-chamber TOF was encoded and read out through a LECROY 4290 system.

The trigger logic for a beam antiproton was

$$\bar{p}=BH\cdot S1\cdot S2\cdot[\mathrm{TOF}(BH\text{-}S1)=20\text{ ns}]\cdot[\mathrm{PH}(S1)=3\times\mathrm{minimum}]\cdot[\mathrm{PH}(S2)=3\times\mathrm{minimum}]\ , \tag{6}$$

where PH=signal pulse height, proportional to the energy loss in the counter and minimum=signal from a minimally ionizing particle. The pion rejection using this trigger was better than 10^5:1. The trigger logic that defined an antineutron annihilation in the target was given by

$$\bar{n}=\bar{p}\cdot M\geq2\cdot(t_m-t_{S2})\geq6\text{ ns}\ , \tag{7}$$

where *M* is the number of *M* counters hit and t_m-t_{S2} is

the TOF between the $S2$ scintillator and the M counters. This requirement rejected the majority of events, which consisted of stopping antiprotons annihilating in the target. The trigger logic for the events of interest was

$$\text{event}=\bar{N}\cdot N \ , \tag{8}$$

where $\bar{N}$ is given above and N is a logic signal from the neutron counter. All events meeting this requirement (about 1 beam $\bar{p}$ in 500) were written to tape, at a rate of 3–5 events per spill. Further details of the electronics and the beam line are given in Refs. 12 and 13.

IV. DATA ANALYSIS

The vertex detectors were used to locate the $\bar{n}$-p annihilation in the LH_2 target. An annihilation vertex was defined by two or more charged-particle tracks which intersected at a common point. In practice the midpoint between the points of closest approach for the projected tracks for each pair of tracks with a distance of closest approach less than 2.5 cm were used. The vertex resolution was approximately ± 1 cm in each dimension. Position information from the M counters was used to eliminate ambiguous and bad track solutions in the vertex reconstruction process. The combined efficiency for vertex reconstruction from a given $\bar{n}$-p annihilation within the target volume is 38.0%. This was estimated by Monte Carlo simulation with all known detector efficiencies and geometries included. The vertex detector subtended approximately 85% of 4π Sr.

The following cuts were applied to select as clean a sample of events as possible in which an antineutron annihilates in the target and the associated neutron from the charge exchange fires one of the neutron counters. First, a vertex inside the LH_2 target was required from the drift chambers. Events in which a second, accidental, antiproton entered the target were rejected with additional time-to-digital converters (TDC's) on the beam counters and the $\bar{p}$ coincidence gate. The following detector elements were required to have a hit: at least one beam hodoscope element, at least two M counters, a single neutron counter, and no veto counters. The average M-counter mean-time had to be at least 6.0 ns later than would be the case for a stopping antiproton annihilation. The neutron-counter time had to be consistent with kinematic constraints on the neutron momentum. A fiducial volume cut corresponding to ± 40.0 cm along the neutron detector was also applied.

All timing was done relative to scintillator $S2$. The TDC offsets for the crucial detectors (i.e., M, neutron, and veto counters) were determined using charged annihilation pions from stopping antiprotons. The accuracy of this calibration for each individual counter element was estimated to be better than 0.5 ns. Whenever possible consistency with beam pions was checked. This comparison between beam and annihilation pions determined the antiproton stopping time from $S2$ to be around 4.0 ns. As a result the start time of the neutron time of flight was uncertain by 2.5–3.0 ns, depending upon the antiproton momentum at the time of charge exchange. Samples of stopping antiprotons were taken throughout the experiment for continuous monitoring of the time calibration.

The time difference between the neutron-counter and the M-counter average (t_n-t_m) was used to eliminate gammas from antineutron annihilations which could have simulated a neutron from charge exchange. Note that with our calibration method these gammas would occur at 0.0 ns in t_n-t_m regardless of the actual annihilation time of the antineutron. Therefore a ± 2.0-ns cut was imposed on this variable t_n-t_m (see Fig. 10 below). The identification of these gammas from antineutron annihilation was verified by looking for showers initiated in the neutron counters (see Fig. 10). This was attempted by requiring no front veto counter and a back veto counter to fire. A strong peak at ~ 0 ns in t_n-t_m was observed corresponding to charged pions from antineutron annihilation hitting the M counters and correlated gammas from π^0's hitting the neutron counters. Also, runs taken with $\frac{1}{8}$ in. of Pb between the front veto and the neutron counters showed a 44% increase in the number of events in a ± 2.0-ns-wide window around $t_n-t_m=0$ relative to the number of counts outside the window.

One remaining cut involved the pulse height in the neutron counters. A lower threshold of 1.0-MeV electron equivalent was chosen in the off-line analysis. This resulted in an efficiency, averaged over energy and path length, of about 30% for the neutrons of interest (10–40 MeV), as determined by the Kent State neutron efficiency code.[14] Since the front veto counters were only about 98% efficient, we also imposed a 30.0-MeV upper threshold in order to reject the few remaining charged pions. This cut had only a very small effect on the statistics of the final sample.

The antineutron momentum at charge exchange was determined from the measured time of flight and position of the neutron-counter hit. The kinematics reconstruction in this experiment contains relatively large uncertainties due to poor knowledge of the charge-exchange point and time, as well as the substantial thickness of the neutron counters (20 cm) with the resulting smearing out of the neutron flight path. The neutron hit was assumed to be the center of the firing counter in the Z and Y directions. The X position was calculated from the difference of the phototube times. The $\bar{p}$ and $\bar{n}$ energies are then reconstructed assuming that the charge-exchange point occurred on the beam axis and 12.5 cm from the front edge of the target. (The beam momentum was chosen so that the antiproton range in the LH_2 was 25 cm.) The formulas used for these calculations are

$$P_{\bar{p}}=\frac{P_n-QM_n/P_n}{\cos\Theta_n} \ \text{MeV}/c \ , \tag{9}$$

$$Q=2.0(M_p-M_n) \ \text{MeV} \ , \tag{10}$$

and

$$P_{\bar{n}}=(P_{\bar{p}}^2+P_n^2-2P_pP_n\cos\Theta_n)^{1/2} \ \text{MeV}/c \ , \tag{11}$$

where the momentum of the neutron is calculated from the TOF. The reconstructed antiproton momentum at charge exchange was required to be between 120 and 375 MeV/c (the kinematically allowed range).

V. MONTE CARLO SIMULATION

The measured quantity $\Delta n_A(t)$, the number of antineutrons annihilating between t and $t+\delta t$, was related to the $\bar{n}p$ scattering length by a Monte Carlo simulation. The basic features of this simulation are as follows. Incident $\bar{p}$'s were propagated through the target simulating energy loss and hadronic interactions. Antineutrons from the charge exchange were propagated through the target simulating hadronic interactions. If annihilation occurred within the LH_2 target, the resulting pions were tracked to verify that the trigger conditions were met. The corresponding neutron was propagated through the target and projected to the neutron counter. Events which satisfied all the trigger conditions were subjected to the same cuts and momentum reconstruction used in the data analysis. The low-energy $\bar{n}p$ cross sections were varied to find the best fit to the data. Various models for the charge-exchange and high-energy $\bar{n}p$ cross sections were tried, to test the sensitivity of the results to these assumptions. Details of the procedure and the assumptions are given below.

The incident $\bar{p}$ phase space was parametrized to reproduce the measured $\bar{p}$ phase space at scintillator $S2$. As in the experiment, $S2$ was taken as the origin of time. The incident $\bar{p}$ beam was then transported through the LH_2 target, taking into account energy loss, annihilation, elastic scattering, and charge exchange. None of the $\bar{p}$'s penetrated the target.

The $\bar{p}$ cross sections were parametrized as[15]

$$\sigma_A = 38.0 + 35.0/P \text{ mb} , \tag{12}$$

$$\sigma_T = 65.8 + 53.8/P \text{ mb} , \tag{13}$$

and

$$\sigma_E = \sigma_T - \sigma_A - \sigma_C \text{ mb} , \tag{14}$$

where P is in units of GeV/c. Two parametrizations were tried for the charge-exchange cross section σ_C:

$$\sigma_C = \frac{17.34[1.0-(0.0986/P)^2]^{1/2}}{1.0-0.45P+2.0P^2} \text{ mb} \tag{15}$$

and

$$\sigma_C = \frac{17.34[1.0-(0.0986/P)^2]^{1/2}}{1.0+2.0P^2} \text{ mb} . \tag{16}$$

The first, Eq. (15), is due to Hamilton *et al.*[16] The second, Eq. (16), is a fit to the data of Bruckner *et al.*[17] and was used below 250 MeV/c. It was then smoothly interpolated to Eq. (15) above 300 MeV/c.

The $\bar{p}p$ elastic differential cross section was calculated using the s-, p-, and d-wave scattering amplitudes from Ref. 18. These amplitudes were determined by fitting[19] the Heidelberg data from 180 to 600 MeV/c. The amplitudes are isospin averaged. The charge-exchange differential cross sections of Ref. 17 were parametrized by

$$\frac{d\sigma}{dt} = Ae^{(b_1+b_2/p^2)t} , \tag{17}$$

where $b_1 = 5.0$ (GeV/c^2)$^{-2}$ and $b_2 = 2.0$. Although this parametrization does not reproduce the structure seen at small $\bar{n}$ angles,[17,20] this does not affect the results since only neutrons near 0° ($\theta_{\bar{n}} \simeq 180°$) are detected in the measurement. This region is well reproduced, as can be seen in Fig. 4.

One percent of the incident $\bar{p}$'s were found to undergo charge exchange. Antineutrons resulting from charge exchanges were then propagated through the LH_2 target. The $\bar{n}$'s were followed until they annihilated or left the target. Antineutrons that left the target were assumed to annihilate far enough away that chamber tracking would eliminate such events from the data set. For $\bar{n}$'s above 100 MeV/c the total, annihilation, and elastic-scattering cross sections and elastic differential $\bar{n}p$ cross sections were calculated using the optical-potential models of either Dover and Richard[21] or Côte *et al.*[22] (Paris group). Dover and Richard used a G-parity transformation of the NN potential of the Paris group, along with a complex phenomenological spin-, isospin-, and energy-independent annihilation potential. The Paris group fit the available $\bar{p}p$ data using a more flexible form for the annihilation potential. This form has no real part as in the Dover-Richard model, but does include an explicit energy dependence. Six parameters were adjusted to give the best fit to the data, and are different for isospin 0 and 1. However, because of the limited amount of data available (especially spin-isospin observables) these parameters were not all uniquely determined.

The $I=1$ cross-section parametrizations used above 100 MeV/c were

$$\sigma_A = 58.2 + 21.9/P \text{ mb (Dover-Richard)} , \tag{18}$$

$$\sigma_T = 118.2 + 28.91/P \text{ mb} , \tag{19}$$

$$\sigma_A = 30.2 + 28.3/P \text{ mb (Paris)} , \tag{20}$$

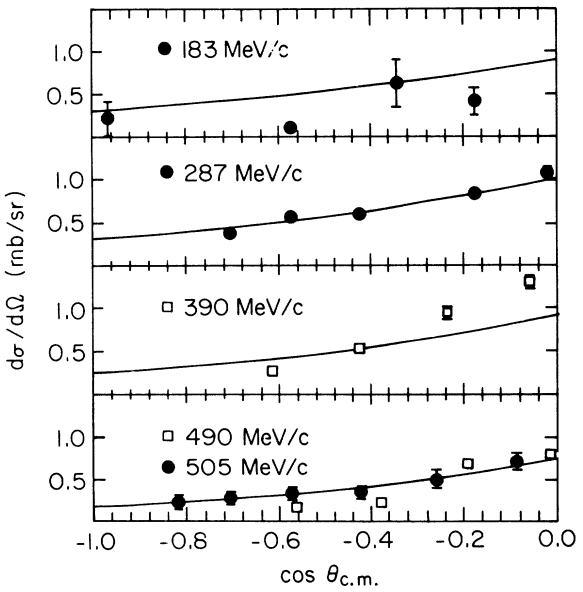

FIG. 4. Back angle $\bar{p}p \to \bar{n}n$ differential cross section. The boxes are the data of Bruckner *et al.* (Ref. 17); the solid circles are the data of Nakamura *et al.* (Ref. 20). The curve is the parametrization of Eqs. (16) and (17).

and

$$\sigma_T = 77.0 + 39.9/P \text{ mb} . \quad (21)$$

The differential cross sections for these two potential modes were calculated at 5.0, 7.5, 10.0, 12.5, 30.0, 50.0, 70.0, 90.0, 110.0, and 130.0 MeV kinetic energy and smoothly interpolated as a function of energy and angle.

For $\bar{n}$'s below 50 MeV/c the $I=1$ annihilation cross section was calculated using the spin-averaged complex scattering length[23]

$$\sigma_A = \frac{-4\pi \, \mathrm{Im} a / |a|^2}{k \, |1/a + ik|^2} \text{ mb} . \quad (22)$$

Between 50 and 100 MeV/c a smooth interpolation was made between the two parametrizations. The elastic cross section was smoothly interpolated to the value at $\sigma_E(0)$.

The Fermi[24] statistical theory was used to determine the distribution of pion multiplicities from $\bar{n}$-p annihilation. The average pion multiplicity was five. The charge correlations of the final states were determined by the "correlation-number" theory of Pais.[25] Given the charge ratios as calculated from the Pais method, and the distribution of multiplicities as calculated from the Fermi method, the branching ratios for the various possible annihilation channels were determined. The momentum four-vectors of the annihilation products were generated uniformly in Lorentz-invariant phase space by a modified version of the program SAGE (Ref. 26). Details of these procedures and comparisons with $\bar{p}p$ and $\bar{n}p$ annihilation data are given in Ref. 27.

The charged annihilation products were then transported through the LH_2, aluminum vacuum vessel, and if appropriate, the scintillation counters M, taking into account energy loss. A valid event required that at least two pions penetrate the M counters and that no pions hit the veto counter. The $\bar{n}$ annihilation time was taken to be the average time of all pion hits on the M counters. This time was smeared with a Gaussian resolution function with a width of 1.2 ns. About 2% of the $\bar{n}$'s led to a valid annihilation. The pions were not tracked through the drift chambers. The probability that they would result in a reconstructable track was taken to be 0.38 (see discussion under Vertex Detector above).

Neutrons from charge exchanges with valid $\bar{n}$ annihilations were then propagated through the LH_2. A parametrization by Gammel[28] was used for the np total cross section. The differential cross section was parametrized by

$$\frac{\partial\sigma}{\partial\Omega} \propto 1 + BP^4 \cos\theta^2 \text{ mb} , \quad (23)$$

where P is the laboratory momentum in GeV/c and $B=85.0$. Once the neutron left the target, it was tracked until it intersected the neutron bars (or not). Neutrons that struck the drift chamber frames were assumed to be totally absorbed. Neutron interactions in the aluminum vacuum vessel and/or the M counters and their light guides, were taken into account through a simple black disc model. Once it was determined that a neutron had struck a neutron bar, the efficiency for neutron detection and the interaction point was calculated. For a threshold of 1 MeV the neutron detection efficiency averaged over energy and path length was found to be 30%. Only about three $\bar{p}$'s in 10^5 produced a valid event.

The Monte Carlo events were then processed in the same manner as the data in order to reproduce the measured distributions. The neutron TOF was smeared with a Gaussian resolution function with a width of 0.8 ns. The Y_n and Z_n coordinates of the neutron were set equal to the center of the neutron bar in which it was detected. The X_n coordinate is smeared with a Gaussian resolution of ± 5 cm. Cuts of ± 40 cm were placed on this coordinate. The calculated $\bar{p}$ momentum was restricted to 120—375 MeV/c. The neutron bar pulse height was restricted to 1.0–30.0 MeV. The absolute value of the difference of the neutron TOF and the $\bar{n}$ annihilation time was required to be greater than ± 2 ns, and the $\bar{n}$ annihilation time was required to be greater than 6.0 ns.

VI. COMPARISON OF DATA WITH MONTE CARLO SIMULATION

The antineutron momentum ($P_{\bar{n}}$) spectrum calculated from the measured neutron time of flight and angle is plotted in Fig. 5, along with the Monte Carlo simulation. The parameters used for the calculations shown in Figs. 5–12 were $\beta\sigma_A(0)=45$ mb and $\sigma_E(0)=200$ mb. The structure in the $\bar{n}$ momentum spectrum is due to the granularity in Θ_n imposed by the limited number of neutron bars. It should be noted that this spectrum is calculated at charge exchange, that is, the $P_{\bar{n}}$ spectrum represents the momentum at which $\bar{n}$'s are produced in the LH_2 target. The antineutrons are produced with momenta from 10 to 75 MeV/c corresponding to $\bar{n}p$ c.m. energies of 0.027–1.3 MeV. The difference of the actual value of $P_{\bar{n}}$ at charge exchange and the value of $P_{\bar{n}}$ calculated from Eq. (11) for Monte Carlo events is plotted in Fig. 6. The FWHM is 18 MeV/c, due primarily to the

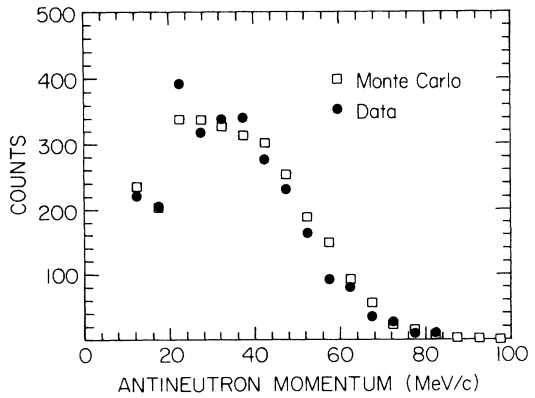

FIG. 5. Antineutron momentum spectrum. Antineutron momentum at charge exchange, calculated from neutron TOF and interaction position in neutron detector using Eq. (11).

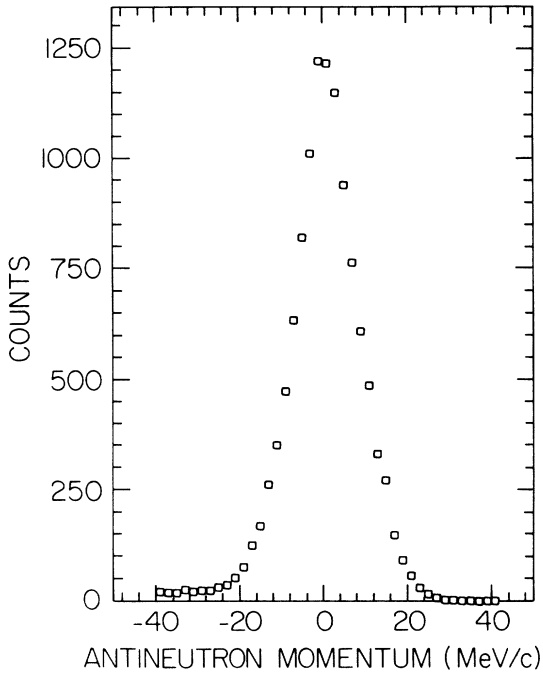

FIG. 6. Monte Carlo antineutron momentum difference. The antineutron momentum minus the antineutron momentum calculated from Eq. (11).

uncertainty in the neutron time of flight. In view of this spread in $P_{\bar{N}}^{\text{calc}}$, it did not seem reasonable to subdivide the antineutron momentum spectrum into fine momentum bins. Instead the data was divided into two bins of P_n^{calc} less than or greater than 40 MeV/c. The Monte Carlo momentum spectra for the antineutrons at the annihilation point are shown in Figs. 7 and 8. They peak at about 22 and 43 MeV/c, corresponding to a c.m. energy

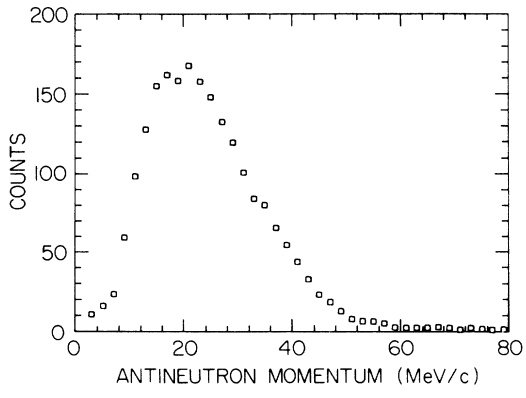

FIG. 7. Monte Carlo antineutron momentum at annihilation for $P_{\bar{n}} \leq 40$ MeV/c.

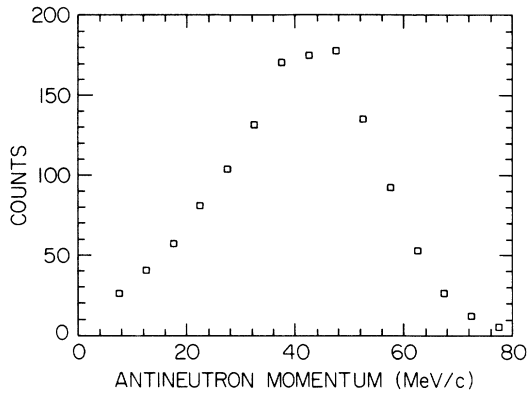

FIG. 8. Monte Carlo antineutron momenta at annihilation for $P_{\bar{n}} \geq 40$ MeV/c.

of 135 and 490 keV.

Further comparisons of the data and the Monte Carlo simulation are shown in Figs. 9–12 for $P_{\bar{n}} \leq 40$ MeV/c. The measured antineutron survival time spectrum t_m is shown in Fig. 9. Counts below $t_m = 6$ ns are suppressed to eliminate the tails of the stopping antiproton annihilation time spectrum. The measured $t_n - t_m$ time spectrum is shown in Fig. 10. The point $t_n - t_m = 0$ corresponds to a neutron TOF of 6 ns, while the average neutron TOF

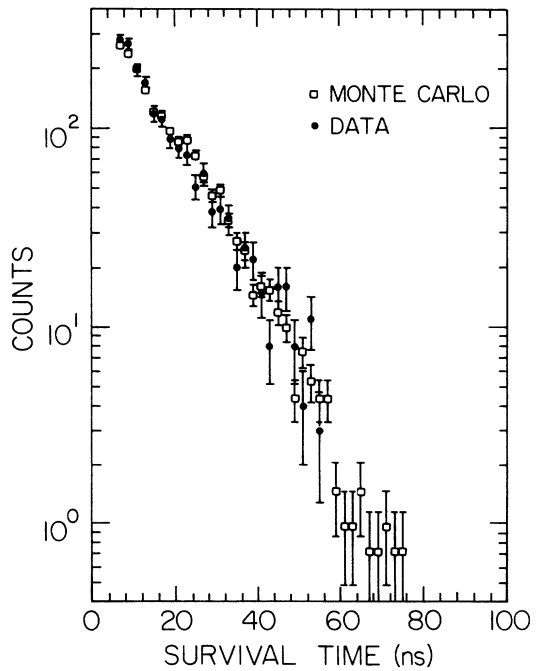

FIG. 9. Antineutron survival time for $P_{\bar{n}} \leq 40$ MeV/c.

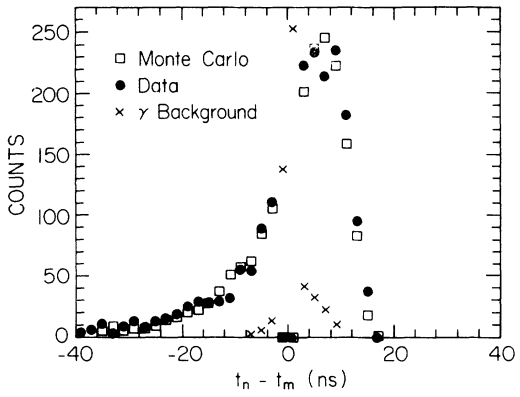

FIG. 10. The neutron TOF minus the antineutron survival time for $P_{\bar{n}} \leq 40$ MeV. The crosses are gamma background events triggered by requiring no hits in the front neutron veto counters and a hit in the neutron counter and the back veto counters.

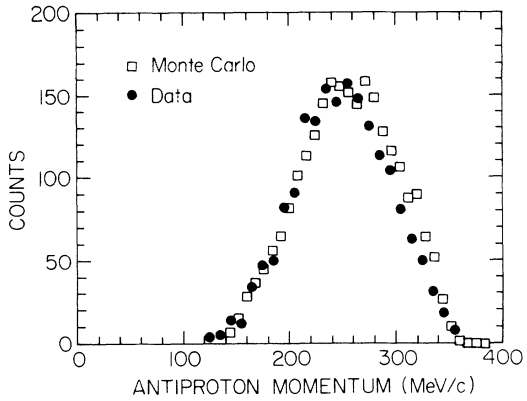

FIG. 12. Antiproton momentum for $P_{\bar{n}} \leq 40$ MeV/c. The incident antiproton momentum at charge exchange is calculated from Eq. (6).

ranges from 17 to 31 ns. The ±2-ns cut imposed on $t_n - t_m$ thus results in a slight loss of events in the t_m spectrum at 18±7 ns, as can be seen in Fig. 9. The X position of the neutron (summed over all bars) is plotted in Fig. 11. The antiproton momentum (P_p) calculated from Eq. (9) is plotted in Fig. 12. The Monte Carlo calculation has a small excess of events around 300 MeV/c. This may be due to more energy loss in the antiproton beam than was accounted for in the Monte Carlo calculation. When combined with the N-counter acceptance and charge-exchange cross section, this results in the small excess of antineutrons above $P_n = 40$ MeV/c seen in Fig. 5. Figures 5 and 9–12 demonstrate that the Monte Carlo simulation reproduces the essential features of the data.

VII. RESULTS AND DISCUSSION

The antineutron survival-time spectrum (t_m) calculated from the Monte Carlo simulation was compared to the data by calculating χ^2 using the t_m data from 6 to 60 ns. The value of $\beta\sigma_A(0)$ was varied in 5-mb steps and $\sigma_E(0)$ was varied in 50-mb steps. This procedure was done for both momentum bins with the two potential models, Dover-Richard and Paris, being used to calculate the $\bar{n}p$ elastic and annihilation cross sections as was discussed in Sec. V. In both cases the charge-exchange cross section was parametrized by Eq. (16) (Bruckner *et al.*[17] normalization). The minimum in χ^2 was estimated by a parabolic fit as shown in Fig. 13. It was found, as expected, that the data are relatively insensitive to the value of $\sigma_E(0)$ with a broad minimum at 221±51 mb. The data determine the value of $\beta\sigma_A$ at $P_{\bar{n}} = 22\pm12$ and 43±15 MeV/c.

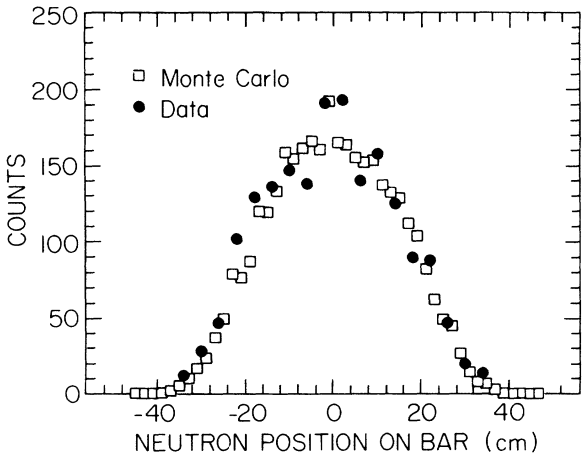

FIG. 11. Neutron interaction position along the neutron detector summed over all bars for $P_{\bar{n}} \leq 40$ MeV/c. The x position is calculated from the time difference of the signals from each end of the scintillator bar.

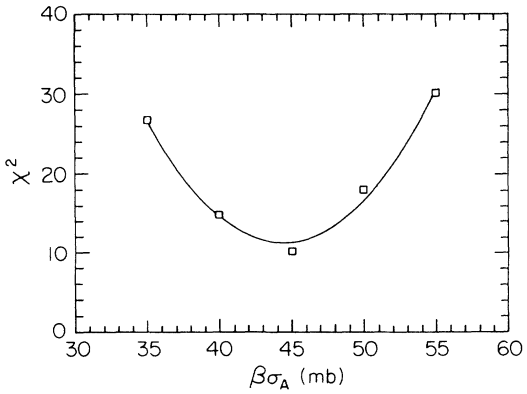

FIG. 13. Plot of χ^2 vs $\beta\sigma_A(0)$ for $P_{\bar{n}} \leq 40$ MeV/c using the Dover-Richard potential model. The curve is a parabolic fit.

TABLE I. Monte Carlo results.

Potential	Charge-exchange normalization	σ_A parametrization	$\beta\sigma_A(22)$ mb	χ^2/DF	$\beta\sigma_A(43)$ mb	χ^2/DF	$\beta\sigma_A(0)$ mb
DR	Eq. (16)	Eq. (18)	40.7±2.8	1.10	32.8±3.6	1.18	44.8±3.1
Paris	Eq. (16)	Eq. (20)	39.6±3.1	1.09	30.9±6.1	1.21	43.5±3.7
DR	Eq. (16)[a]	Eq. (18)	39.7±3.1	1.18	33.0±4.4	1.25	43.6±3.4
DR	Eq. (15)	Eq. (18)	41.2±3.2	1.24	31.2±5.9	1.32	45.4±3.5

[a]Isotropic

The results for $\beta\sigma_A(22)$ and $\beta\sigma_A(43)$ are given in Table I for various parametrizations of the input data, as discussed below. The value for $\beta\sigma_A(0)$, extrapolated from $\beta\sigma_A(22)$ is also given. The errors quoted are one sigma ($\chi^2_{\min}+1$). The values of of $\beta\sigma_A(22)$ vary by about ±1 mb and $\beta_A(43)$ by about ±1.5 mb, while the statistical errors are approximately ±3 and ±5 mb, respectively. Thus the results are insensitive to the Monte Carlo input parameters.

The systematic errors are hard to estimate, but they are probably dominated by the uncertainty in the charge-exchange cross section near threshold. There are no direct measurements in the energy and angular range used in this experiment. (See Fig. 4.) However the extrapolation from higher energies and smaller angles have reproduced the measured $P_{\bar{n}}$ and $P_{\bar{p}}$ spectra, giving considerable confidence in the quoted results. A test of the effect of a different extrapolation of the total charge-exchange cross section near threshold was done by using Eq. (15) (Hamilton *et al.*[16] normalization). The resulting values of $\beta\sigma_A$ are given in Table I. They agree with the other results to within the stated errors. The potential models were not used to estimate the charge-exchange differential cross sections since they did not reproduce the existing data well. Instead the fits to the higher-energy data were smoothly extrapolated to isotropy at threshold. The effect of this approximation was tested by using an isotropic charge-exchange differential cross section for all energies. The results, listed in Table I, still agree within errors. We conclude from these studies that the results are not seriously affected by the approximations made in the Monte Carlo simulation. We find $\beta\sigma_A(22)=40\pm3$ mb and $\beta\sigma_A(43)=32\pm5$ mb. The value of $\beta\sigma_A(0)=44\pm3.5$ mb was extrapolated from $\beta\sigma_A(22)$. The systematic error is estimated to be about 1 mb.

The values of $\beta\sigma_A$ are plotted in Fig. 14 along with the values of $\beta\sigma_A$ at higher energies measured in the only other existing $\bar{n}$-p experiments.[7,8] The horizontal error bar denotes the momentum range of our data. The present results and the previous measurement by this group, Armstrong *et al.*,[8] are in reasonable agreement. The solid curve was calculated from the Dover-Richard potential and the dashed curve from the Paris potential. The calculations bracket our result, with the Paris potential giving the better agreement. The dip structure in both models is explained by referring to Fig. 15 where the

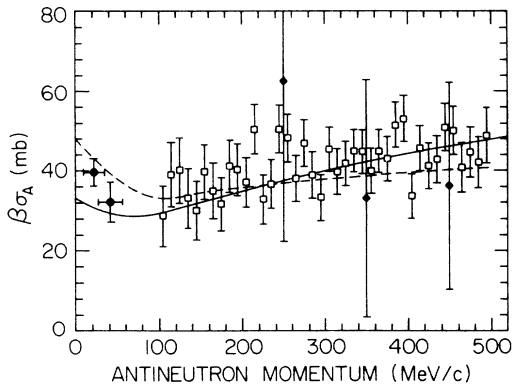

FIG. 14. Plot of $\beta\sigma_A$ vs $P_{\bar{n}}$. The solid circles are the present result. The horizontal error bars indicate the momentum range of the data. The open squares are the data of Armstrong *et al.* (Ref. 8) and the diamonds are the data of Gunderson *et al.* (Ref. 7) both from $\bar{n}p$ transmission experiments. The solid curve is the prediction of the Dover-Richard potential (Ref. 21) and the dashed curve is the prediction of the Paris potential (Ref. 22).

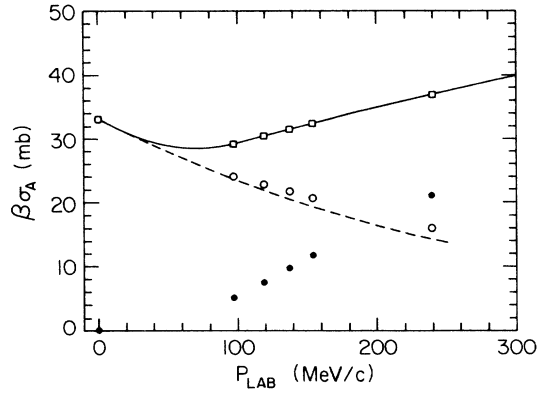

FIG. 15. Plot of $\beta\sigma_A$ calculated from the Dover-Richard potential vs antineutron laboratory momentum. The open squares are the total annihilation cross section, the open circles are the *S*-wave partial cross section, and the solid circles are the *P*-wave partial cross section. The solid curve is as given in Fig. 14 and the dashed curve is the scattering length approximation calculated from Eq. (22).

TABLE II. $\bar{N}N$ scattering lengths: theory.

Potential	Ref.	$I=0$ a_0 (fm)	$I=1$ a_1 (fm)	$\bar{p}p$ $a_{\bar{p}p}$ (fm)
BPI	1	$1.17-i0.87$	$0.83-i0.64$	$1.00-i0.75$
BPII	1	$0.91-i0.82$	$0.87-i0.80$	$0.89-i0.81$
Paris	22	$1.02-i0.68$	$1.04-i0.91$	$1.03-i0.79$
DR	21	$0.86-i0.88$	$0.94-i0.63$	$0.90-i0.75$

annihilation cross section is decomposed into its partial waves. The symbols are the calculated values of $\beta\sigma_A$ for the total cross section and for the S- and P-wave partial cross sections at 0.0, 5.0, 7.5, 10.0, 12.5, and 30 MeV for the Dover-Richard potential. The dashed curve is calculated from Eq. (22) using the Dover-Richard scattering length, while the solid curve is a smooth extrapolation between Eq. (22) below 50 MeV/c and Eq. (18) above 100 MeV/c. Since this model does not give any S-wave resonances near threshold, the scattering length approximation reproduces the low-energy S-wave partial cross section. The total annihilation cross section is already deviating from the S waves below 100 MeV/c and the dip in $\beta\sigma_A$ is thus caused by the large amount of P waves at low energy.

The value of $\beta\sigma_A(0)$ determined in this experiment corresponds to an imaginary part of the $I=1$ spin-averaged S-wave scattering length of

$$\mathrm{Im}a_1=-0.83\pm0.07 \text{ fm} , \tag{24}$$

where again the errors quoted are one sigma. The only previous determination of the $I=1$ scattering length is from the $\bar{p}$-^{16}O, ^{18}O atomic data by Poth *et al.*[6] They found

$$a_1=0.3\pm1.4-i(1.0\pm1.7) \text{ fm} . \tag{25}$$

Our results represent a substantial improvement. The values of a_1, as well as a_0 and $a_{\bar{p}p}$, calculated from various potential models are listed in Table II. The theories bracket the measured value. The scattering length is sensitive to the tail of the real part of the potential outside the strong absorption region, about 1.1 fm. The inclusion of the current data, and the data of Armstrong *et al.*, in the existing $\bar{N}$-N data set should lead to a set of potential parameters that would significantly improve the fit to the low-energy $I=1$ data.

The $I=0$ spin-averaged S-wave scattering length can be calculated from the above result and the $a_{\bar{p}p}$ scattering length deduced from $\bar{p}$-p atomic data. The existing measurements of the complex energy shifts of the protonium atomic levels are given in Table III. Comparing the values of the complex energy shifts calculated by Moussalam[29] (Paris potential) or Richard and Sainio[30] (Dover-Richard potential) and the weighted average of the data given in Table III, the $a_{\bar{p}p}$ scattering length can be estimated as

$$a_{\bar{p}p}=0.93\pm0.09-i(0.95\pm0.12) \text{ fm} . \tag{26}$$

The $I=0$ scattering length is given by

$$a_0=2a_{\bar{p}p}-a_1 \tag{27}$$

which gives

$$\mathrm{Im}a_0=-1.07\pm0.16 \text{ fm} . \tag{28}$$

This value is larger than the range of theoretical values primarily because the measured value of $a_{\bar{p}p}$ is larger than the values listed in Table II.

A comparison of the $\bar{p}p$ and $\bar{n}p$ ($\bar{p}n$) annihilation cross sections is given in Fig. 16. The ratio of the imaginary part of the a_1 to the imaginary part of the $a_{\bar{p}p}$ scattering lengths gives this quantity at zero energy. The ratio of the $\bar{n}p$ annihilation data of Armstrong *et al.*[8] to the $\bar{p}p$ data of Bruckner *et al.*[19] below 300 MeV/c and Brando *et al.*[31] above 300 MeV/c is shown at higher energies. The predictions of the Dover-Richard potential and Paris potential are shown as solid and dashed curves, respectively. The potential calculations are in good agreement with the data. Again the scattering length value is bracketed by the calculations, with the Dover-Richard poten-

TABLE III. Complex energy shifts of the protonium levels in keV.

	Ref.	ΔE_R	$\Gamma/2$
Data	Gorringe (Ref. 4)	0.71 ± 0.08	-0.64 ± 0.10
Data	Bacher (Ref. 5)	0.66 ± 0.13	-0.56 ± 0.11
	Weighted average	0.696 ± 0.068	-0.60 ± 0.074
Theory	Dover and Richard (Ref. 30)	0.70	-0.47
Theory	Paris group (Ref. 29)	0.75	-0.50

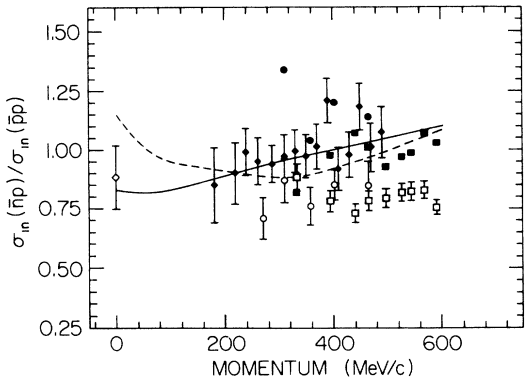

FIG. 16. Plot of the ratio of the annihilation cross sections for the $\bar{n}p$ ($\bar{p}n$) to $\bar{p}p$ interactions vs $\bar{n}$ ($\bar{p}$) laboratory momentum. The open diamond is the ratio of the $\bar{n}p/\bar{p}p$ scattering lengths (see text). The solid diamonds are the ratio of the $\bar{n}p$ data of Armstrong *et al.* (Ref. 8) to the $\bar{p}p$ data of Bruckner *et al.* (Ref. 19) below 300 MeV/c and Brando *et al.* (Ref. 32) above 300 MeV/c. The ratio $\bar{p}n/\bar{p}p$ from the $\bar{p}$D bubble-chamber data of Kalogeropoulos and Tzanakos (Ref. 10) are denoted by open circles and the data of Bizzarri *et al.* (Ref. 9) by open squares. The corresponding ratios corrected for rescattering effects using Glauber theory are shown as solid circles (Ref. 32) and solid squares (Ref. 33). The solid curve is the prediction of the Dover-Richard potential (Ref. 21) and the dashed curve is the prediction of the Paris potential (Ref. 22).

tial in slightly better agreement, primarily because of the large value of $a_{\bar{p}p}$. The ratio of the $\bar{p}n$ to $\bar{p}p$ cross sections has been measured in $\bar{p}$-D experiments by Kalogeropoulos and Tzanakos[10] and Bizzarri *et al.*[9] These data are plotted in Fig. 16 along with the corresponding ratio corrected for rescattering effects using Glauber theory.[32,33] These corrections improve the agreement with theory for the Bizzarri data, but tend to overcorrect the Kalogeropoulos and Tzanakos data. The three different types of measurements are in general agreement with the potential model predictions of the cross-section ratios.

In summary, we have measured the survival time spectrum of slow antineutrons produced in a LH_2 target. This is the first tagged $\bar{n}$ experiment. From the data we have deduced the imaginary part of the $I=1$, spin-averaged S-wave scattering length for antineutron-proton interactions. The result lies within the range of values calculated from various potential models. The results represent a substantial improvement over existing $I=1$ data. In addition, by combining our results with the average for $a_{\bar{p}p}$ we have deduced a value for the imaginary part of the $I=0$ $\bar{N}N$ spin-averaged S-wave scattering length.

ACKNOWLEDGMENTS

The authors wish to express their appreciation to the AGS Staff and especially to D. Lazarus and W. McGahern. We would also like to thank C.B. Dover and J.-M. Richard for many helpful discussions of their potential model calculations. This work was supported by the U.S. Department of Energy under Contracts Nos. DE-FG-87ER4030 (Rice) and DE-AS-05-76ER03948 (University of Houston). The work at Pennsylvania State was supported in part by the National Science Foundation. Travel support for Professor M. Furic was supplied from the U.S.-Yugoslavia Joint Fund (NSF Grant No. 681).

[1]R. A. Bryan and R. J. N. Phillips, Nucl. Phys. **B5**, 201 (1968).
[2]F. Myhrer and A. W. Thomas, Phys. Lett. **64B**, 54 (1976).
[3]S. Ahmad *et al.*, Phys. Lett. **157B**, 333 (1985); in *Proceedings of the 8th European Symposium on Nucleon-Nucleon Interactions,* Thessaloniki, 1986, edited by S. Charalambous *et al.* (World Scientific, Singapore, 1987), p. 205.
[4]T. P. Gorringe *et al.*, Phys. Lett. **162B**, 71 (1986); C. A. Baker *et al.*, in *PANIC '87,* proceedings of the Eleventh International Conference on Particles and Nuclei, Kyoto, Japan, 1987, edited by S. Homma *et al.* [Nucl. Phys. **A478**, 1c-914c (1988)] (North-Holland, Amsterdam, 1988); W. J. C. Okx *et al.*, Nucl. Instrum. Methods **A252**, 605 (1986).
[5]R. Bacher *et al.*, in *Proceedings of the 8th European Symposium on Nucleon-Nucleon Interactions* (Ref. 3).
[6]H. Poth *et al.*, Nucl. Phys. **A294**, 435 (1978).
[7]B. Gunderson *et al.*, Phys. Rev. D **23**, 587 (1981).
[8]T. Armstrong *et al.*, Phys. Rev. D **36**, 659 (1987).
[9]R. Bizzarri *et al.*, Nuovo Cimento **22A**, 225 (1974).
[10]T. E. Kalogeropoulos and G. S. Tzanakos, Phys. Rev. D **22**, 2585 (1980).
[11]J. Rosner, in *New Directions in Hadron Spectroscopy,* proceedings of the Summer Symposium, Argonne, 1975, edited by S. L. Kramer and E. L. Berger (ANL, Argonne, 1975), p. 165.
[12]A. T. Hicks, Ph.D. dissertation, Pennsylvania State University, 1986.
[13]Y. Y. Xue, Ph.D. dissertation, University of Houston, 1985.
[14]R. A. Cecil *et al.*, Nucl. Instrum. Methods **161**, 439 (1979); S. Cierjacks *et al, ibid.* **192**, 405 (1982).
[15]C. Beard *et al.*, in *Antiproton 1984,* proceedings of the VII European Symposium on Antiproton Interactions, Durham, England, 1984, edited by M. R. Pennington (Inst. Phys. Conf. Ser. No. 73) (Hilger, Bristol, 1985), p. 147.
[16]R. Hamilton *et al.*, Phys. Rev. Lett. **44**, 1182 (1980).
[17]W. Bruckner *et al.*, Phys. Lett. **169B**, 302 (1986).
[18]R. Ransome (private communication).
[19]W. Bruckner *et al.*, Phys. Lett. **166B**, 113 (1986); **158B**, 180 (1985).
[20]K. Nakamura *et al.*, Phys. Rev. Lett. **53** 885 (1984); T. Kageyama *et al.*, Phys. Rev. D **35**, 2655 (1987).
[21]C. B. Dover and J.-M. Richard, Phys. Rev. C **21**, 1466 (1980).
[22]J. Côte *et al.*, Phys. Rev. Lett. **48**, 1319 (1982).
[23]G. F. Chew and J. Koplik, Nucl. Phys. **B79**, 365 (1974).
[24]E. Segre, Annu. Rev. Nucl. Sci. **8**, 127 (1960); A. Ekspong *et al.*, Nucl. Phys. **22**, 353 (1961), and references therein.

[25]A. Pais, Ann. Phys. (N.Y.) **9**, 548 (1960).
[26]J. Friedman, J. Comp. Phys. **7**, 201 (1971).
[27]R. Moss, M. A. thesis, Rice University, 1985.
[28]J. Gammel, in *Fast Neutron Physics Part II,* edited by J. B. Marion and J. L. Fowler (Interscience, New York, 1963), p. 2209.
[29]B. Moussallam, Z. Phys. **325A**, 1 (1986).
[30]J.-M. Richard and M. E. Sainio, Phys. Lett. **110B**, 349 (1982).
[31]T. Brando *et al.*, Phys. Lett. **158B**, 505 (1985).
[32]L. A. Kondratyuk, Yad. Fiz. **24**, 477 (1976) [Sov. J. Nucl. Phys. **24**, 247 (1976)].
[33]L. A. Kondratyuk and M. Zh. Shmatikov, Phys. Lett. **117B**, 381 (1982).